IEEE Access
Multidisciplinary | Rapid Review | Open Access Journal

Received January 18, 2017, accepted February 13, 2017, date of publication March 1, 2017, date of current version May 17, 2017.

*Digital Object Identifier 10.1109/ACCESS.2017.2671440*

# Adaptive Sliding Mode Relative Motion Control for Autonomous Carrier Landing of Fixed-Wing Unmanned Aerial Vehicles

**ZEWEI ZHENG[1], (Member, IEEE), ZHENGHAO JIN[2,3], LIANG SUN[1], (Member, IEEE), AND MING ZHU[2]**

[1]Seventh Research Division, Science and Technology on Aircraft Control Laboratory, Beihang University, Beijing 100191, China
[2]School of Aeronautic Science and Engineering, Beihang University, Beijing 100191, China
[3]Tianjin Zhong Wei Aerospace Data System Technology Co., Ltd, Tianjin 300301, China

Corresponding author: Z. Jin (jinzhenghao@buaa.edu.cn)

This work was supported in part by the National Natural Science Foundation of China under Grant 61503010, in part by the China Postdoctoral Science Foundation under Grant 2016M590031, in part by the Aeronautical Science Foundation of China under Grant 2016ZA51001, and in part by the Fundamental Research Funds for the Central Universities under Grant YWF-16-GJSYS-02.

**ABSTRACT** In this paper, relative motion model and control strategy for autonomous fixed-wing unmanned aerial vehicle (UAV) carrier landing are addressed. First, a coupled six-degrees-of-freedom (6-DOF) non-linear relative motion model is established from 6-DOF UAV and carrier models. Second, because of the under-actuated characteristic of two vehicles, the 6-DOF relative motion model is simplified to a four-degree-of-freedom (4-DOF) model to facilitate the control design. Third, an adaptive sliding mode control law is proposed to track desired landing trajectory and maintain constant relative pitch and roll angles. Finally, simulation results demonstrate the effectiveness of the proposed control method.

**INDEX TERMS** Carrier landing control, fixed-wing UAV, adaptive sliding mode, 4-DOF control.

## I. INTRODUCTION

The autonomous fixed-wing UAV carrier landing control technology is served as a vital premise for UAV carrier and UAV fulfilling the tasks. Meanwhile, automatic landing technology is also so complicated that it can not be conquered easily. In order to reduce the carrier landing deviation, some methods have been applied to model and control design. In term of model, most of landing models are built on the basis of a single UAV model. Some technologies or methods have been applied to control system, such as deck motion compensation technology, power compensation link, automatic throttle control, direct lift control technology. In the early stage of carrier landing control technology, the classical control methods were adopted to automatic landing systems. The automatic landing system was developed for nearly half a century, the basic structure of the system got little change. With the maturity of the classical control theory, especially the theory and method of frequency domain analysis, the stability of automatic landing carrier have a large progress. Moreover, most of the automatic landing controls only concern about attitude loop control.

In recent years, based on the single UAV model, many nonlinear control methods were proposed in carrier landing systems. In the field of control design, the latest research works mainly focus on optimizing parameters [1]–[3], improving the control accuracy and robustness of the dynamic inversion control system [4], [5], improving the accuracy of sensor [6], reducing the noise of radar tracking and radio data link [7]. In addition, the fuzzy control method [8] was introduced into control system. In [9]–[11], it was considered the control of height and pitch angle for landing carrier by designing a fuzzy PID flight control system, but the application of the control law is limited and only developed for the pitch angle under a given height motion. In [12], a dynamic inversion attitude control law was proposed by using 6-DOF aircraft model. From the recently studies, there are little change in the model. However, in the aspect of space docking, some scholars have tried to use the relative motion mode [13] to achieve the relative motion control design. Moreover, it is rare to take the relative motion model into consideration by means of carrier landing control law. The probable reason is that the 6-DOF carrier model [14], [15] is very complicated for control design. Therefore, the corresponding 6-DOF relative motion model control law is hard to design. So simplification is inevitable for fulfilling the desired controller [16].

This paper mainly illustrates the control problem of the autonomous fixed-wing UAV carrier landing by relative motion model. The main contributions of this paper are stated as follows. Firstly, based on the 6-DOF models of fixed-wing UAV and carrier, a 6-DOF relative motion model is established for the autonomous fixed-wing UAV carrier landing missions. Taking the under-actuated property of the controlled fixed wing aircraft into account, the proposed 6-DOF relative motion model is simplified into a 4-DOF fully actuated relative motion model to facilitate the control design. Secondly, in order to assure the desired landing trajectory, constant relative pitch and roll angles, and lateral position and velocity, a sliding mode control law [17] is designed for autonomous landing missions. Moreover, the uncertainty parameters [18] and unknown external disturbances [19] are considered in control design, then an adaptive control method is combined with sliding mode control approach to compensate mode uncertainties. Thirdly, it is proved that the designed controller ensures that the relative position and attitude errors converge to zero, and the simulation example verifies the feasibility of the proposed method.

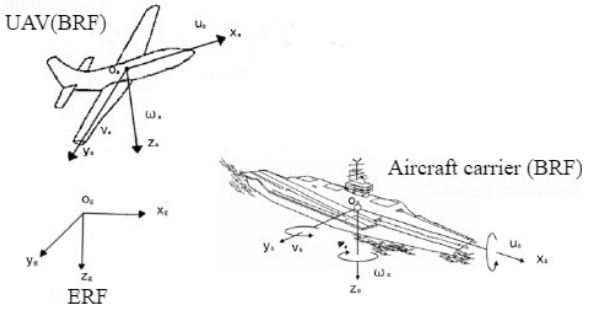


**FIGURE 1.** Structure of the UAV and aicraft carrier.

## II. PROBLEM STATEMENT

As shown in Fig. 1, $\mathbb{F}_g \triangleq \{o_g, x_g, y_g, z_g\}$ denotes the Earth reference frame(ERF), where $O_g$ is the origin on the surface of the Earth, $o_g x_g$ points to the north, $o_g y_g$ points to the east, and $o_g z_g$ points vertically down along the gravity vector. $\mathbb{F}_a \triangleq \{o_a, x_a, y_a, z_a\}$ denotes the UAV body-fixed reference frame(BRF), where the origin $O_a$ is fixed to the centre of gravity of the UAV, $o_a x_a$ points to the forward of the UAV, $o_a y_a$ points to the right of the UAV, $o_a z_a$ completes the right-hand orthogonal coordinate system. Similarly, $\mathbb{F}_s \triangleq \{o_s, x_s, y_s, z_s\}$ denotes the carrier body-fixed reference frame, where the origin $o_s$ is fixed with the centre of gravity of the carrier, $o_s x_s$ points to the forward of the carrier, $o_s y_s$ points to the right of the carrier, $o_s z_s$ completes the right-hand orthogonal coordinate system. The model of the UAV carrier landing design in this study is formulated based on the models of the UAV and the carrier. Thus, the 6-DOF mathematical model of UAV and aircraft carrier need to be established firstly. Before setting up the model of UAV and carrier, it is assumed that the travel distance of the UAV and carrier is relatively small compared with the dimensions of the Earth. Then, the earth curvature is ignored and the surface of earth is assumed to be flat.

### A. UAV MOTION MODEL

The kinematics of UAV are described by [20]

$$\begin{bmatrix} \dot{\boldsymbol{p}}_a^E \\ \dot{\boldsymbol{\Theta}}_a^E \end{bmatrix} = \boldsymbol{R}_{bg} \begin{bmatrix} \boldsymbol{v}_a \\ \boldsymbol{\Omega}_a \end{bmatrix} \tag{1}$$

where position $\boldsymbol{p}_a^E = [x_a, y_a, z_a]^T$ and euler angle $\boldsymbol{\Theta}_a^E = [\phi_a, \theta_a, \psi_a]^T$ are defined in ERF; velocity $\boldsymbol{v}_a = [u_a, v_a, w_a]^T$ and angular velocity $\boldsymbol{\Omega}_a = [p_a, q_a, r_a]^T$ are defined in BRF. $\boldsymbol{R}_{bg}$ is represented by

$$\boldsymbol{R}_{bg} = \begin{bmatrix} \boldsymbol{R}_a & 0_{3\times3} \\ 0_{3\times3} & \boldsymbol{K}_a \end{bmatrix} \tag{2}$$

where $\boldsymbol{R}_a$ is the direction cosine matrix of BRF to ERF; $\boldsymbol{K}_a$ is the Jacobian matrix, and

$$\begin{aligned} \boldsymbol{R}_a &= \begin{bmatrix} c\theta_a c\psi_a & r_{12}^a & r_{13}^a \\ c\theta_a s\psi_a & r_{22}^a & r_{23}^a \\ -s\theta_a & c\theta_a s\phi_a & c\theta_a c\phi_a \end{bmatrix} \\ \boldsymbol{K}_a &= \begin{bmatrix} 1 & t\theta_a s\phi_a & t\theta_a c\phi_a \\ 0 & c\phi_a & -s\phi_a \\ 0 & s\phi_a/c\theta_a & c\phi_a/c\theta_a \end{bmatrix} \end{aligned} \tag{3}$$

where $s(x)$, $c(x)$ and $t(x)$ are short for $\sin(x)$, $\cos(x)$, $\tan(x)$, respectively; $r_{12}^a = s\theta_a c\psi_a s\phi_a - s\psi_a c\phi_a$, $r_{13}^a = s\theta_a c\psi_a c\phi_a + s\psi_a s\phi_a$, $r_{22}^a = s\theta_a s\psi_a s\phi_a + c\psi_a c\phi_a$, $r_{23}^a = s\theta_a s\psi_a c\phi_a - c\psi_a s\phi_a$.

The dynamics of UAV in $\mathbb{F}_a$ are described by

$$\begin{cases} m_a[\dot{\boldsymbol{v}}_a + \boldsymbol{S}(\boldsymbol{\Omega}_a)\boldsymbol{v}_a] = \boldsymbol{F}_a + \boldsymbol{d}_f \\ \boldsymbol{I}_a\dot{\boldsymbol{\Omega}}_a + \boldsymbol{S}(\boldsymbol{\Omega}_a)\boldsymbol{I}_a\boldsymbol{\Omega}_a = \boldsymbol{M}_a + \boldsymbol{d}_\tau \end{cases} \tag{4}$$

where $m_a \in \mathbb{R}$ is the whole mass of the UAV. The moment of inertia and the products of inertia are described by

$$\boldsymbol{I}_a = \begin{bmatrix} I_x & 0 & -I_{xz} \\ 0 & I_y & 0 \\ -I_{zx} & 0 & I_z \end{bmatrix} \tag{5}$$

$\boldsymbol{S}(\boldsymbol{\Omega}_a)$ is the skew-symmetric matrix for $\boldsymbol{\Omega}_a \in \mathbb{R}^3$; $\boldsymbol{d}_f, \boldsymbol{d}_\tau \in \mathbb{R}^3$ are disturbance force and torque respectively; the external force $\boldsymbol{F}_a = [F_x, F_y, F_z]^T$ is defined by

$$\begin{aligned} F_x &= X_u u_a + X_w w_a + X_q q_a + X_{\delta_T}\delta_T + X_{\delta_e}\delta_e \\ &\quad - m_a g\sin\theta_a \\ F_y &= Y_v v_a + Y_p p_a + Y_r r_a + Y_{\delta_a}\delta_a + Y_{\delta_r}\delta_r \\ &\quad + mm_a g\sin\phi_a\cos\theta_a \\ F_z &= Z_u u_a + Z_w w_a + Z_q q_a + Z_{\delta_T}\delta_T + Z_{\delta_e}\delta_e \\ &\quad + m_a g\cos\phi_a\cos\theta_a \end{aligned} \tag{6}$$

where $\delta_T$, $\delta_a$, $\delta_e$, $\delta_r$, and $g$ denotes the thrust, aileron, elevator, rudder, and gravity, respectively; $X_i$, $Y_j$, $Z_k (i = u, w, q, r, \delta_T, \delta_a, \delta_e; j = v, p, r, \delta_a, \delta_r; k = u, w, q, \delta_T, \delta_e)$

are aerodynamic derivatives. The aerodynamic moment $\boldsymbol{M}_a = [L, M, N]^T$ is defined by

$$\begin{aligned} L &= L_v v_a + L_p p_a + L_r r_a + L_{\delta_a}\delta_a + L_{\delta_r}\delta_r \\ M &= M_u u_a + M_w w_a + M_q q_a + M_{\delta_T}\delta_T + M_{\delta_e}\delta_e \\ N &= N_v v_a + N_p p_a + N_r r_a + N_{\delta_a}\delta_a + N_{\delta_r}\delta_r \end{aligned} \tag{7}$$

and the $L_i, M_j, N_k (i = v, p, r, \delta_a, \delta_r; j = u, w, q, \delta_T, \delta_e; k = v, p, r, \delta_a, \delta_r)$ are aerodynamic derivatives.

### B. CARRIER MOTION MODEL

The kinematics of carrier are described by [14]

$$\begin{bmatrix} \dot{\boldsymbol{p}}_s^E \\ \dot{\boldsymbol{\Theta}}_s^E \end{bmatrix} = \boldsymbol{\mathcal{D}} \begin{bmatrix} \boldsymbol{R}_s & 0_{3\times3} \\ 0_{3\times3} & \boldsymbol{K}_s \end{bmatrix} \begin{bmatrix} \boldsymbol{v}_s \\ \boldsymbol{\Omega}_s \end{bmatrix} \tag{8}$$

where position $\boldsymbol{p}_s^E = [x_s, y_s, z_s]^T$ and euler angle $\boldsymbol{\Theta}_s^E = [\phi_s, \theta_s, \psi_s]^T$ are defined in ERF; velocity $\boldsymbol{v}_s = [u_s, v_s, w_s]^T$ and angular velocity $\boldsymbol{\Omega}_s = [p_s, q_s, r_s]^T$ are defined in carrier's BRF. $\boldsymbol{R}_s$ is the direction cosine matrix of carrier's BRF to ERF; $\boldsymbol{K}_s$ is the Jacobian matrix, and

$$\begin{aligned} \boldsymbol{R}_s &= \begin{bmatrix} c\theta_s c\psi_s & r_{12}^s & r_{13}^s \\ c\theta_s s\psi_s & r_{22}^s & r_{23}^s \\ -s\theta_s & c\theta_s s\phi_s & c\theta_s c\phi_s \end{bmatrix} \\ \boldsymbol{K}_s &= \begin{bmatrix} 1 & t\theta_s s\phi_s & t\theta_s c\phi_s \\ 0 & c\phi_s & -s\phi_s \\ 0 & s\phi_s/c\theta_s & c\phi_s/c\theta_s \end{bmatrix} \end{aligned} \tag{9}$$

where $r_{12}^s = s\theta_s c\psi_s s\phi_s - s\psi_s c\phi_s$, $r_{13}^s = s\theta_s c\psi_s c\phi_s + s\psi_s s\phi_s$,$r_{22}^s = s\theta_s s\psi_s s\phi_s + c\psi_s c\phi_s$, $r_{23}^s = s\theta_s s\psi_s c\phi_s - c\psi_s s\phi_s$, respectively.

The dynamics of carrier are described by [21]–[23]

$$\begin{cases} \dot{u}_s = \dfrac{m_{22}}{m_{11}} v_s r_s - \dfrac{d_{11}}{m_{11}} u_s + \dfrac{1}{m_{11}} \tau_u \\ \dot{v}_s = -\dfrac{m_{11}}{m_{22}} u_s r_s - \dfrac{d_{22}}{m_{22}} v_s + \dfrac{1}{m_{22}} \\ \dot{w}_s = \zeta_1 \sin(\omega_1 t) + \zeta_2 \sin(\omega_2 t) \\ \dot{p}_s = \zeta_3 \sin(\omega_3 t) + \zeta_4 \sin(\omega_4 t) + b_1 \\ \dot{q}_s = \zeta_5 \sin(\omega_5 t) + \zeta_6 \sin(\omega_6 t) + b_2 \\ \dot{r}_s = \dfrac{m_{11} - m_{22}}{m_{33}} u_s v_s - \dfrac{d_{33}}{m_{33}} r + \dfrac{1}{m_{33}} \tau_r \end{cases} \tag{10}$$

where $m_{11} = m_s - X_{\dot{u}}, m_{22} = m_s - Y_{\dot{v}}, m_{33} = I_z - N_{\dot{r}}$, $d_{11} = -X_u, d_{22} = -Y_v, d_{33} = -N_r$, $m_{ii}$ are the mass and inertia model terms with $m_d = m_{22} - m_{11} > 0$. The term $m_{ii}$ includes additional mass generated by hydraulic pressure forces and torque due to forced harmonic motion of the vessel. The model term $d_{ii}$ represents the hydrodynamic damping forces related with the corresponding velocities in general. $X_{\dot{u}}, Y_{\dot{v}}, Y_{\dot{r}}, Y_{\dot{v}}, X_u, Y_v, N_r$ represent the additional mass constants. The surge force $\tau_u$ and yaw moment $\tau_r$ are provided by two actuators actuated on the carrier. $\zeta_1, \zeta_2, \omega_1, \omega_2$ is the vertical motion coefficient in different sea conditions; $\zeta_3, \zeta_4, b_1, \omega_3, \omega_4$ is the rolling motion coefficient in different sea conditions; $\zeta_5, \zeta_6, b_2, \omega_5, \omega_6$ is the pitching motion coefficient in different sea conditions.

### C. RELATIVE MOTION MODEL

The relative position and relative attitude in ERF can be described by [24]

$$\begin{bmatrix} \boldsymbol{p}_e^E \\ \boldsymbol{\Theta}_e^E \end{bmatrix} = \begin{bmatrix} \boldsymbol{p}_a^E \\ \boldsymbol{\Theta}_a^E \end{bmatrix} - \begin{bmatrix} \boldsymbol{p}_s^E \\ \boldsymbol{\Theta}_s^E \end{bmatrix} \tag{11}$$

Thus, the relative kinematics are presented from the UAV's kinematics by

$$\begin{bmatrix} \dot{\boldsymbol{p}}_e^E \\ \dot{\boldsymbol{\Theta}}_e^E \end{bmatrix} = \boldsymbol{R}_{bg} \begin{bmatrix} \boldsymbol{v}_e \\ \boldsymbol{\Omega}_e \end{bmatrix} \tag{12}$$

where $\boldsymbol{p}_e^E$ is the relative position in ERF; $\boldsymbol{\Theta}_e^E$ is the relative attitude in ERF; $\boldsymbol{v}_e$ is the relative velocity in UAV's BRF; $\boldsymbol{\Omega}_e$ is the relative angular velocity in UAV's BRF.

The relative velocity and relative angular velocity expressed in BRF are

$$\begin{bmatrix} \boldsymbol{v}_e \\ \boldsymbol{\Omega}_e \end{bmatrix} = \begin{bmatrix} \boldsymbol{v}_a \\ \boldsymbol{\Omega}_a \end{bmatrix} - \boldsymbol{R}_s^a \begin{bmatrix} \boldsymbol{v}_s \\ \boldsymbol{\Omega}_s \end{bmatrix} \tag{13}$$

where

$$\boldsymbol{R}_s^a = \begin{bmatrix} \boldsymbol{R}_{sa} & 0_{3\times3} \\ 0_{3\times3} & \boldsymbol{R}_{sa} \end{bmatrix} \tag{14}$$

and $\boldsymbol{R}_{sa} = \boldsymbol{R}_a^T \boldsymbol{R}_s$ is the direction cosine matrix of carrier's BRF to UAV's BRF.

Taking the time derivative of the relative velocity and relative angular velocity in (13) results in the 6-DOF relative motion model as

$$\begin{bmatrix} \dot{\boldsymbol{v}}_e \\ \dot{\boldsymbol{\Omega}}_e \end{bmatrix} = \begin{bmatrix} \dot{\boldsymbol{v}}_a \\ \dot{\boldsymbol{\Omega}}_a \end{bmatrix} - \dot{\boldsymbol{R}}_s^a \begin{bmatrix} \boldsymbol{v}_s \\ \boldsymbol{\Omega}_s \end{bmatrix} - \boldsymbol{R}_s^a \begin{bmatrix} \dot{\boldsymbol{v}}_s \\ \dot{\boldsymbol{\Omega}}_s \end{bmatrix} \tag{15}$$

where $\dot{\boldsymbol{v}}_e$ is the relative acceleration, $\dot{\boldsymbol{\Omega}}_e$ is the relative angular acceleration.

Due to the under-actuated property of the fixed-wing aircraft in the control aspect, this 6-DOF relative motion model should be simplified to 4-DOF relative motion model. Because the lateral displacement $y_a$ of the fixed-wing aircraft is associated with the yaw angle $\psi_a$, and the vertical velocity $w_a$ is related to the forward velocity $u_a$ in the autonomous landing missions. Therefore, to ensure the successful landing missions, the 6-DOF relative model is simplified as 4-DOF relative model, such as relative lateral displacement $y_e$, relative vertical displacement $z_e$, relative rolling $\phi_e$, and pitching attitude $\theta_e$. Thus, the 4-DOF relative kinematics and dynamics are presented by [18], [19]

$$\begin{cases} \dot{\boldsymbol{x}}_1 = \boldsymbol{R}_b^e \boldsymbol{x}_2 \\ \dot{\boldsymbol{x}}_2 = \boldsymbol{f}(\boldsymbol{x}) + \boldsymbol{B}\boldsymbol{u} + \boldsymbol{d} \end{cases} \tag{16}$$

where $\boldsymbol{x}_1 = [y_e, z_e, \phi_e, \theta_e]^T$, $\boldsymbol{x}_2 = [v_e, w_e, p_e, q_e]^T$; $\boldsymbol{R}_b^e$ is simplified from $\boldsymbol{R}_{bg}$ to a $4 \times 4$ rotation matrix,

$$\boldsymbol{R}_b^e = \begin{bmatrix} r_{22}^a & r_{23}^a & 0 & 0 \\ c\theta_a s\phi_a & c\theta_a s\phi_a & 0 & 0 \\ 0 & 0 & 1 & t\theta_a s\phi_a \\ 0 & 0 & 0 & c\phi_a \end{bmatrix}$$

$$\boldsymbol{B} = \begin{bmatrix} 0 & \frac{Y_{\delta_r}}{m_a} & \frac{Y_{\delta_a}}{m_a} & 0 \\ \frac{Z_{\delta_T}}{m_a} & 0 & 0 & \frac{Z_{\delta_e}}{m_a} \\ 0 & \frac{I_z L_{\delta_r} + I_{xz} N_{\delta_r}}{I_x I_z - I_{xz}^2} & \frac{I_z L_{\delta_a} + I_{xz} N_{\delta_a}}{I_x I_z - I_{xz}^2} & 0 \\ \frac{M_{\delta_T}}{I_y} & 0 & 0 & \frac{M_{\delta_e}}{I_y} \end{bmatrix}$$

$$\boldsymbol{u} = [u_1 \;\; u_2 \;\; u_3 \;\; u_4]^T = [\delta_T \;\; \delta_r \;\; \delta_a \;\; \delta_e]^T$$

$$\boldsymbol{f}(\boldsymbol{x}) = \begin{bmatrix} \frac{1}{m_a}\bar{F}_y \\ \frac{1}{m_a}\bar{F}_z \\ \dot{\bar{p}}_a \\ \dot{\bar{q}}_a \end{bmatrix} - \boldsymbol{R}_s^e \begin{bmatrix} \dot{v}_s \\ \dot{w}_s \\ \dot{p}_s \\ \dot{q}_s \end{bmatrix} - \boldsymbol{S}\boldsymbol{R}_s^e \begin{bmatrix} v_s \\ w_s \\ p_s \\ q_s \end{bmatrix}$$

$\boldsymbol{R}_s^e$ is simplified from $\boldsymbol{R}_s^a$ to be a $4 \times 4$ rotation matrix; $\boldsymbol{S}$ and $\boldsymbol{R}_s^e$ can be presented by

$$\boldsymbol{S} = \begin{bmatrix} s_{11} & s_{12} & 0 & 0 \\ s_{21} & s_{22} & 0 & 0 \\ 0 & 0 & s_{11} & s_{12} \\ 0 & 0 & s_{21} & s_{22} \end{bmatrix} \tag{17}$$

$$\boldsymbol{R}_s^e = \begin{bmatrix} h_{11} & h_{12} & 0 & 0 \\ h_{21} & h_{22} & 0 & 0 \\ 0 & 0 & h_{11} & h_{12} \\ 0 & 0 & h_{21} & h_{22} \end{bmatrix} \tag{18}$$

with $s_{11} = -q_a c\theta_s s\phi_a + (c\theta_a c\psi_a^2 s\theta_a + c\theta_a s\psi_a^2 s\theta_a)p_a + 2\psi_a r_a c\psi_a c\theta_a s\theta_a s\phi_a - s\theta_a c\theta_s p_s$, $s_{12} = -q_a c\theta_s c\phi_s + (c\theta_a s\phi_a c\psi_a + 2c\theta_a \psi_a s\theta_a c\phi_a)r_a + p_a(c\theta_a c\psi_a - c\theta_a s\psi_a c\psi_a)$, $s_{21} = p_a(s\theta_a c\psi_a r_{12}^s + s\theta_a s\psi_a r_{22}^s + c\theta_a c\theta_s s\phi_s) + q_a(c\psi_a s\phi_a r_{12}^s + s\psi_a s\phi_a r_{22}^s) + r_a(s\theta_a s\phi_a r_{22}^s - c\phi_a r_{12}^s)$, $s_{22} = p_a(s\theta_a c\psi_a r_{13}^s + s\theta_a s\psi_a r_{23}^s + c\theta_a c\theta_s c\phi_s) + q_a(c\psi_a s\phi_a r_{13}^s + s\psi_a s\phi_a r_{23}^s) + r_a(s\theta_a s\phi_a r_{23}^s - c\phi_a r_{13}^s)$, and $h_{11} = c\theta_a c\psi_a r_{12}^s + c\theta_a s\psi_a r_{22}^s - s\theta_a c\theta_s s\phi_s$, $h_{12} = c\theta_a c\psi_a r_{13}^s + c\theta_a s\psi_a r_{23}^s - s\theta_a c\theta_s c\phi_s$, $h_{21} = r_{12}^a r_{12}^s + r_{22}^a r_{22}^s + c\theta_a s\phi_a c\theta_s s\phi_s$, $h_{22} = r_{12}^a r_{13}^s + r_{22}^a r_{23}^s + c\theta_a s\phi_a c\theta_s c\phi_s$, respectively. Moreover, $\bar{F}_y$, $\bar{F}_z$, $\dot{\bar{p}}_a$, and $\dot{\bar{q}}_a$ are denoted by

$$\begin{aligned} \bar{F}_y &= (Y_v v_a + Y_p p_a + Y_r r_a + mg \sin\phi_a \cos\theta_a) - u_a r_a \\ &\quad + p_a w_a \\ \bar{F}_z &= (Z_u u_a + Z_w w_a + Z_q q_a + mg \cos\phi_a \cos\theta_a) \\ &\quad - p_a v_a + u_a q_a \\ \dot{\bar{p}}_a &= \frac{1}{I_x I_z - I_{xz}^2}[(I_z(L_v v_a + L_p p_a + L_r r_a) \\ &\quad + I_{xz}(N_v v_a + N_p p_a + N_r r_a)) + I_{xz}(I_x + I_z - I_y)p_a q_a \\ &\quad - (I_z^2 + I_{xz}^2 - I_y I_z)q_a r_a \\ \dot{\bar{q}}_a &= \frac{1}{I_y}[M_u u_a + M_w w_a + M_q q_a + (I_z \\ &\quad - I_x)p_a r_a + I_{xz}(r_a{}^2 - p_a{}^2)] \end{aligned} \tag{19}$$

and $\boldsymbol{d}_\tau, \boldsymbol{d}_f \in \mathbb{R}^3$ are also simplified as $\boldsymbol{d}_{\tau s}, \boldsymbol{d}_{fs} \in \mathbb{R}^2$, respectively [25].

*Remark 1:* In terms of navigation, the accuracy of positioning technology for UAV autonomous carrier landing is very high. RTK (Real Time Kinematic) technology can meet the requirement of positioning accuracy. Unlike other positioning techniques, the RTK directly obtain the relative position data of the UAV and the aircraft carrier by calculating, rather than their respective position coordinates. So the accuracy of RTK technology can reach centimeter level. This is one of the reasons why this paper uses the relative motion model.

*Assumption 1:* The aerodynamic and control parameters can be presented by $\varepsilon_i = \varepsilon_{i0} + \varepsilon_{i\Delta}$, where $\varepsilon \triangleq X, Y, Z, L, M, N$; $i \triangleq \delta_a, \delta_e, \delta_e, \delta_r, u, v, w, p, q, r$. $\varepsilon_{i0}$ are known constants and $\varepsilon_{i\Delta}$ are unknown and bounded scalars.

*Assumption 2:* The external disturbance $\boldsymbol{d}_f$ and $\boldsymbol{d}_\Delta$ are unknown but bounded by $\|\boldsymbol{d}\| \leq d_m$ with an unknown constant $d_m$.

### D. CONTROL OBJECT

The control objective in this work is to drive the UAV tracking the carrier a certain position. The control aim of the autonomous landing missions is that the relative vertical position $z_e$ tracks to desired trajectory $z_e^c$, and the relative lateral position $y_e$, velocity $v_e$, roll angle $\phi_e$, and pitch angle $\theta_e$ track to $y_e^c$, $v_e^c$, $\phi_e^c$, $\theta_e^c$, respectively. Thus, the control objective aims to design a control input $\boldsymbol{u}$ under Assumptions 1 and 2, such that the controlled tracking with model can guarantee $\lim_{t\to\infty}\boldsymbol{x}_1 = \boldsymbol{x}_1^c$, where $\boldsymbol{x}_1^c = [y_e^c, z_e^c, \phi_e^c, \theta_e^c]^T$,

## III. CONTROLLER DESIGN

The relative motion controller is presented based on an adaptive sliding mode design method. Adaptive laws are derived to compensate the parametric uncertainties and restrain the external environment disturbances in model [26].

Define a sliding surface [27]

$$\boldsymbol{s} = \dot{\tilde{\boldsymbol{x}}}_1 + a\tilde{\boldsymbol{x}}_1 \tag{20}$$

where $\tilde{\boldsymbol{x}}_1 = \boldsymbol{x}_1 - \boldsymbol{x}_1^c$, $a \geq 0$.

Differentiating (20) with (16) leaves

$$\begin{aligned} \dot{\boldsymbol{s}} &= \ddot{\tilde{\boldsymbol{x}}}_1 + a\dot{\tilde{\boldsymbol{x}}}_1 \\ &= \ddot{\boldsymbol{x}}_1 + a(\dot{\boldsymbol{x}}_1 - \dot{\boldsymbol{x}}_1^c) \\ &= \dot{\boldsymbol{R}}_b^e \boldsymbol{x}_2 + \boldsymbol{R}_b^e[\boldsymbol{f}(\boldsymbol{x}) + \boldsymbol{B}\boldsymbol{u} + \boldsymbol{d}] + a\dot{\tilde{\boldsymbol{x}}}_1 \end{aligned} \tag{21}$$

According to Assumption 1, we know the term $\boldsymbol{f}(\boldsymbol{x})$ can be divided into $\boldsymbol{f}(\boldsymbol{x}) = \boldsymbol{f}_0 + \boldsymbol{f}_\Delta$ and $\boldsymbol{B}$ can be divided into $\boldsymbol{B}\,\mathcal{D}\,\boldsymbol{B}_0 + \boldsymbol{B}_\Delta$. Then, Eq. (21) becomes

$$\dot{\boldsymbol{s}} = \dot{\boldsymbol{R}}_b^e(\boldsymbol{R}_b^e)^{-1}\dot{\boldsymbol{x}}_1 + \boldsymbol{R}_b^e[\boldsymbol{f}_0 + \boldsymbol{f}_\Delta + (\boldsymbol{B}_0 + \boldsymbol{B}_\Delta)\boldsymbol{u}\,\mathcal{C}\boldsymbol{d}] + a\dot{\tilde{\boldsymbol{x}}}_1 \tag{22}$$

Introducing a linear operator $\boldsymbol{L}(\boldsymbol{a}_1) \in \mathbb{R}^{4\times 15}$ for any vector $\boldsymbol{a}_1 = [u_a, v_a, w_a, p_a, q_a, r_a]^T$ results in a matrix (23), as shown at the top of the next page, where $s_1 = \frac{I_z}{I_x I_z - I_{xz}^2}$, $s_2 = \frac{I_{xz}}{I_x I_z - I_{xz}^2}$. Then, $\boldsymbol{f}_\Delta = \boldsymbol{L}(\boldsymbol{a}_1)\boldsymbol{\vartheta}_\Delta$, where $\boldsymbol{\vartheta}_\Delta \triangleq [Y_{v\Delta}, Y_{p\Delta}, Y_{r\Delta}, Z_{u\Delta}, Z_{w\Delta}, Z_{q\Delta}, L_{v\Delta}, L_{p\Delta}, L_{r\Delta}, N_{v\Delta}, N_{p\Delta}, N_{r\Delta}, M_{u\Delta}, M_{w\Delta}, M_{q\Delta}]^T$. Similarly, introducing a linear operator $\boldsymbol{M}(\boldsymbol{a}_2) \in \mathbb{R}^{4\times 10}$ for any

$$\boldsymbol{L}(\boldsymbol{a}_1)=\begin{bmatrix} \frac{v_a}{m_a} & \frac{p_a}{m_a} & \frac{r_a}{m_a} & 0 & 0 & 0 & 0 & 0 & 0 & 0 & 0 & 0 & 0 & 0 & 0 \\ 0 & 0 & 0 & \frac{u_a}{m_a} & \frac{w_a}{m_a} & \frac{q_a}{m_a} & 0 & 0 & 0 & 0 & 0 & 0 & 0 & 0 & 0 \\ 0 & 0 & 0 & 0 & 0 & 0 & s_1v_a & s_1p_a & s_1r_a & s_2v_a & s_2p_a & s_2r_a & 0 & 0 & 0 \\ 0 & 0 & 0 & 0 & 0 & 0 & 0 & 0 & 0 & 0 & 0 & 0 & \frac{u_a}{I_y} & \frac{w_a}{I_y} & \frac{q_a}{I_y} \end{bmatrix} \tag{23}$$

$$\boldsymbol{M}(\boldsymbol{a}_2)=\begin{bmatrix} \frac{u_2}{m_a} & \frac{u_3}{m_a} & 0 & 0 & 0 & 0 & 0 & 0 & 0 & 0 \\ 0 & 0 & \frac{u_1}{m_a} & \frac{u_4}{m_a} & 0 & 0 & 0 & 0 & 0 & 0 \\ 0 & 0 & 0 & 0 & s_1u_2 & s_1u_3 & s_2u_2 & s_2u_3 & 0 & 0 \\ 0 & 0 & 0 & 0 & 0 & 0 & 0 & 0 & \frac{u_1}{I_y} & \frac{u_4}{I_y} \end{bmatrix} \tag{24}$$

vector $\boldsymbol{a}_2 = [u_1, u_2, u_3, u_4]^T$ results in a matrix (24), as shown at the top of the next page, Thus, $\boldsymbol{B}_\Delta\boldsymbol{u} = \boldsymbol{M}(\boldsymbol{a}_2)\boldsymbol{\varphi}_\Delta$, where $\boldsymbol{\varphi}_\Delta \triangleq [Y_{\delta_{r\Delta}}, Y_{\delta_{a\Delta}}, Z_{\delta_{T\Delta}}, Z_{\delta_{e\Delta}}, L_{\delta_{r\Delta}}, L_{\delta_{a\Delta}}, N_{\delta_{r\Delta}}, N_{\delta_{a\Delta}}, M_{\delta_{r\Delta}}, M_{\delta_{a\Delta}}]^T$. Then Eq. (22) becomes

$$\begin{aligned}\dot{\boldsymbol{s}} = {} & \dot{\boldsymbol{R}}_b^e(\boldsymbol{R}_b^e)^{-1}\dot{\boldsymbol{x}}_1 + \boldsymbol{R}_b^e[\boldsymbol{f}_0 + \boldsymbol{L}(\boldsymbol{a}_1)\boldsymbol{\vartheta}_\Delta + \boldsymbol{B}_0\boldsymbol{u} \\ & + \boldsymbol{M}(\boldsymbol{a}_2)\boldsymbol{\varphi}_\Delta + \boldsymbol{d}] + a\ddot{\boldsymbol{x}}_1\end{aligned} \tag{25}$$

Define estimation errors $\tilde{\boldsymbol{\vartheta}}_\Delta = \hat{\boldsymbol{\vartheta}}_\Delta - \boldsymbol{\vartheta}_\Delta, \tilde{\boldsymbol{\varphi}}_\Delta = \hat{\boldsymbol{\varphi}}_\Delta - \boldsymbol{\varphi}_\Delta$, $\tilde{d}_m = \hat{d}_m - d_m$, $\boldsymbol{B}_\Delta = \hat{\boldsymbol{B}}_\Delta - \tilde{\boldsymbol{B}}_\Delta$, and choose a Lyapunov function

$$V = \frac{1}{2}\boldsymbol{s}^T\boldsymbol{s} + \frac{1}{2\gamma_1}\tilde{\boldsymbol{\vartheta}}_\Delta^T\tilde{\boldsymbol{\vartheta}}_\Delta + \frac{1}{2\gamma_2}\tilde{\boldsymbol{\varphi}}_\Delta^T\tilde{\boldsymbol{\varphi}}_\Delta + \frac{1}{2\gamma_3}\tilde{d}_m^2 \tag{26}$$

with $\gamma_i > 0 (i = 1, 2, 3)$. Then, taking time derivative of (26) leads to

$$\dot{V} = \boldsymbol{s}^T\dot{\boldsymbol{s}} + \frac{1}{\gamma_1}\tilde{\boldsymbol{\vartheta}}_\Delta^T\dot{\tilde{\boldsymbol{\vartheta}}}_\Delta + \frac{1}{\gamma_2}\tilde{\boldsymbol{\varphi}}_\Delta^T\dot{\tilde{\boldsymbol{\varphi}}}_\Delta + \frac{1}{\gamma_3}\tilde{d}_m\dot{\tilde{d}}_m \tag{27}$$

Substituting (25) into (27) gives

$$\begin{aligned}\dot{V} = {} & \boldsymbol{s}^T[\boldsymbol{R}_b^e\boldsymbol{f}_0 + \boldsymbol{R}_b^e\boldsymbol{L}(\boldsymbol{a}_1)\boldsymbol{\vartheta}_\Delta + \boldsymbol{R}_b^e\boldsymbol{B}_0\boldsymbol{u} \\ & + \boldsymbol{R}_b^e\boldsymbol{M}(\boldsymbol{a}_2)\boldsymbol{\varphi}_\Delta + \boldsymbol{R}_b^e\boldsymbol{d} + \dot{\boldsymbol{R}}_b^e(\boldsymbol{R}_b^e)^{-1}\dot{\boldsymbol{x}}_1 + a\ddot{\boldsymbol{x}}_1] \\ & + \frac{1}{\gamma_1}\tilde{\boldsymbol{\vartheta}}_\Delta^T\dot{\hat{\boldsymbol{\vartheta}}}_\Delta + \frac{1}{\gamma_2}\tilde{\boldsymbol{\varphi}}_\Delta^T\dot{\hat{\boldsymbol{\varphi}}}_\Delta + \frac{1}{\gamma_3}\tilde{d}_m\dot{\hat{d}}_m\end{aligned} \tag{28}$$

Since $\boldsymbol{B}_\Delta = \hat{\boldsymbol{B}}_\Delta - \tilde{\boldsymbol{B}}_\Delta = \boldsymbol{M}(\boldsymbol{a}_2)\hat{\boldsymbol{\varphi}}_\Delta - \boldsymbol{M}(\boldsymbol{a}_2)\tilde{\boldsymbol{\varphi}}_\Delta$, then Eq. (28) becomes

$$\begin{aligned}\dot{V} = {} & \boldsymbol{s}^T[\boldsymbol{R}_b^e\boldsymbol{f}_0 + \boldsymbol{R}_b^e\boldsymbol{L}(\boldsymbol{a}_1)\boldsymbol{\vartheta}_\Delta + \boldsymbol{R}_b^e(\boldsymbol{B}_0 + \hat{\boldsymbol{B}}_\Delta)\boldsymbol{u} \\ & - \boldsymbol{R}_b^e\boldsymbol{M}(\boldsymbol{a}_2)\tilde{\boldsymbol{\varphi}}_\Delta + \boldsymbol{R}_b^e\boldsymbol{d} + \dot{\boldsymbol{R}}_b^e(\boldsymbol{R}_b^e)^{-1}\dot{\boldsymbol{x}}_1 + a\ddot{\boldsymbol{x}}_1] \\ & + \frac{1}{\gamma_1}\tilde{\boldsymbol{\vartheta}}_\Delta^T\dot{\hat{\boldsymbol{\vartheta}}}_\Delta + \frac{1}{\gamma_2}\tilde{\boldsymbol{\varphi}}_\Delta^T\dot{\hat{\boldsymbol{\varphi}}}_\Delta + \frac{1}{\gamma_3}\tilde{d}_m\dot{\hat{d}}_m\end{aligned} \tag{29}$$

Designing the adaptive sliding mode control input as

$$\begin{aligned}\boldsymbol{u} = {} & [\boldsymbol{R}_b^e(\boldsymbol{B}_0 + \hat{\boldsymbol{B}}_\Delta)]^{-1}[-\boldsymbol{R}_b^e(\boldsymbol{f}_0 + \boldsymbol{L}(\boldsymbol{a}_1)\hat{\boldsymbol{\vartheta}}_\Delta) \\ & - \hat{d}_m\|\boldsymbol{R}_b^e\|\mathrm{sgn}(\boldsymbol{s}) - \boldsymbol{k}_1\boldsymbol{s} - a\dot{\tilde{\boldsymbol{x}}}_1 - \dot{\boldsymbol{R}}_b^e(\boldsymbol{R}_b^e)^{-1}\dot{\boldsymbol{x}}_1]\end{aligned} \tag{30}$$

where $\mathrm{sgn}(\boldsymbol{s}) = [sgn(s_1), sgn(s_2), sgn(s_3), sgn(s_4)]^T$, and $sgn(s_i)$ denotes the signum function defined by

$$sgn(s_i) = \begin{cases} 1, & s_i > 0 \\ 0, & s_i = 0 \\ -1, & s_i < 0 \end{cases} \quad i = 1, 2, 3, 4 \tag{31}$$

$\hat{\boldsymbol{B}}_\Delta$ can be presented by

$$\hat{\boldsymbol{B}}_\Delta = \begin{bmatrix} 0 & \frac{\hat{Y}_{\delta_r}}{m_a} & \frac{\hat{Y}_{\delta_a}}{m_a} & 0 \\ \frac{\hat{Z}_{\delta_T}}{m_a} & 0 & 0 & \frac{\hat{Z}_{\delta_e}}{m_a} \\ 0 & \frac{I_z\hat{L}_{\delta_r} + I_{xz}\hat{N}_{\delta_r}}{I_xI_z - I_{xz}^2} & \frac{I_z\hat{L}_{\delta_a} + I_{xz}\hat{N}_{\delta_a}}{I_xI_z - I_{xz}^2} & 0 \\ \frac{\hat{M}_{\delta_T}}{I_y} & 0 & 0 & \frac{\hat{M}_{\delta_e}}{I_y} \end{bmatrix} \tag{32}$$

and diagonal feedback gain matrix $\boldsymbol{k}_1 = diag[k_1, k_2, k_3, k_4]$, $\boldsymbol{k}_1 = \boldsymbol{k}_1^T$. Then substituting (30) into (29) gives

$$\begin{aligned}\dot{V} = {} & \boldsymbol{s}^T[\boldsymbol{R}_b^e\boldsymbol{f}_0 + \boldsymbol{R}_b^e\boldsymbol{f}_\Delta + \boldsymbol{R}_b^e\boldsymbol{d} + \dot{\boldsymbol{R}}_b^e(\boldsymbol{R}_b^e)^{-1}\dot{\boldsymbol{x}}_1 \\ & + a\dot{\tilde{\boldsymbol{x}}}_1 - \boldsymbol{R}_b^e\boldsymbol{f}_0 - \boldsymbol{R}_b^e\boldsymbol{L}(\boldsymbol{a}_1)\hat{\boldsymbol{\vartheta}}_\Delta \\ & - \hat{d}_m\|\boldsymbol{R}_b^e\|\mathrm{sgn}(\boldsymbol{s}) - \boldsymbol{k}_1\boldsymbol{s} - a\dot{\tilde{\boldsymbol{x}}}_1 - \dot{\boldsymbol{R}}_b^e(\boldsymbol{R}_b^e)^{-1}\dot{\boldsymbol{x}}_1 \\ & - \boldsymbol{R}_b^e\boldsymbol{M}(\boldsymbol{a}_2)\tilde{\boldsymbol{\varphi}}_\Delta] + \frac{1}{\gamma_1}\tilde{\boldsymbol{\vartheta}}_\Delta^T\dot{\hat{\boldsymbol{\vartheta}}}_\Delta \\ & + \frac{1}{\gamma_2}\tilde{\boldsymbol{\varphi}}_\Delta^T\dot{\hat{\boldsymbol{\varphi}}}_\Delta + \frac{1}{\gamma_3}\tilde{d}_m\dot{\hat{d}}_m\end{aligned} \tag{33}$$

Assign the update laws for unknown parameters as

$$\begin{cases} \dot{\hat{\boldsymbol{\vartheta}}}_\Delta = \gamma_1(\boldsymbol{R}_b^e\boldsymbol{L}(\boldsymbol{a}_1))^T\boldsymbol{s} \\ \dot{\hat{\boldsymbol{\varphi}}}_\Delta = \gamma_2(\boldsymbol{R}_b^e\boldsymbol{M}(\boldsymbol{a}_2))^T\boldsymbol{s} \\ \dot{\hat{d}}_m = \gamma_3\|\boldsymbol{s}\|_1\|\boldsymbol{R}_b^e\| \end{cases} \tag{34}$$

*Remark 2:* Eq. (34) gives adaptive estimation laws for the unknown parameters $\boldsymbol{\vartheta}_\Delta, \boldsymbol{\varphi}_\Delta, d_m$, the control input $\boldsymbol{u}$ can be derived before updating the estimations of unknown parameters with the given initial estimations.

Substituting (34) into (33) and using properties $\boldsymbol{s}^T\mathrm{sgn}(\boldsymbol{s}) = \|\boldsymbol{s}\|_1$ result in

$$\begin{aligned}\dot{V} \le {} & \boldsymbol{s}^T[\boldsymbol{R}_b^e\boldsymbol{f}_0 + \boldsymbol{R}_b^e\boldsymbol{L}(\boldsymbol{a}_1)\boldsymbol{\vartheta}_\Delta + d_m\|\boldsymbol{R}_b^e\|\mathrm{sgn}(\boldsymbol{s}) \\ & + \dot{\boldsymbol{R}}_b^e(\boldsymbol{R}_b^e)^{-1}\dot{\boldsymbol{x}}_1 + a\dot{\tilde{\boldsymbol{x}}}_1 - \boldsymbol{R}_b^e\boldsymbol{f}_0 - \boldsymbol{R}_b^e\boldsymbol{L}(\boldsymbol{a}_1)\hat{\boldsymbol{\vartheta}}_\Delta \\ & - \hat{d}_m\|\boldsymbol{R}_b^e\|\mathrm{sgn}(\boldsymbol{s}) - \boldsymbol{k}_1\boldsymbol{s} - a\dot{\tilde{\boldsymbol{x}}}_1 - \dot{\boldsymbol{R}}_b^e(\boldsymbol{R}_b^e)^{-1}\dot{\boldsymbol{x}}_1 \\ & - \boldsymbol{R}_b^e\boldsymbol{M}(\boldsymbol{a}_2)\tilde{\boldsymbol{\varphi}}_\Delta] + \tilde{\boldsymbol{\vartheta}}_\Delta^T(\boldsymbol{R}_b^e\boldsymbol{L}(\boldsymbol{a}_1))^T\boldsymbol{s}\end{aligned}$$

$$
\begin{aligned}
&+\tilde{\boldsymbol{\varphi}}_{\Delta}^{T}(\boldsymbol{R}_{b}^{e}\boldsymbol{M}(\boldsymbol{a}_2))^{T}\boldsymbol{s}+\tilde{d}_m\|\boldsymbol{s}\|_1\|\boldsymbol{R}_{b}^{e}\| \\
\leq\ & -\boldsymbol{s}^{T}\boldsymbol{k}_1\boldsymbol{s}-\boldsymbol{s}^{T}\boldsymbol{R}_{b}^{e}\boldsymbol{L}(\boldsymbol{a}_1)\tilde{\boldsymbol{\vartheta}}_{\Delta}+\tilde{\boldsymbol{\vartheta}}_{\Delta}^{T}(\boldsymbol{R}_{b}^{e}\boldsymbol{L}(\boldsymbol{a}_1))^{T}\boldsymbol{s} \\
&-\boldsymbol{s}^{T}\boldsymbol{R}_{b}^{e}\boldsymbol{M}(\boldsymbol{a}_2)\tilde{\boldsymbol{\varphi}}_{\Delta}+\tilde{\boldsymbol{\varphi}}_{\Delta}^{T}(\boldsymbol{R}_{b}^{e}\boldsymbol{M}(\boldsymbol{a}_2))^{T}\boldsymbol{s} \\
&-\tilde{d}_m\|\boldsymbol{s}\|_1\|\boldsymbol{R}_{b}^{e}\|+\tilde{d}_m\|\boldsymbol{s}\|_1\|\boldsymbol{R}_{b}^{e}\| \\
\leq\ & -\boldsymbol{s}^{T}\boldsymbol{k}_1\boldsymbol{s}\leq-\mu\|\boldsymbol{s}\|^2\leq 0
\end{aligned}
\tag{35}
$$

where $\mu=\lambda_{min}(\boldsymbol{k}_1)$, and $\lambda_{min}(\boldsymbol{k}_1)$ is the minimum eigenvalue of matrix.

*Remark 3:* Because of the dynamic coupling between relative position and relative attitude, the changing of a single control parameter can affect multiple states, such that the varying controller parameter $k_1$ have an influence on the convergence of the relative lateral displacement $y_e$ and rolling angle $\phi_e$. The decrease of $k_2$ will aggravate the shock of vertical velocity curve. The rise or fall of $k_4$ will affect the convergence of the relative pitch angle $\theta_e$.

*Theorem 1:* Consider the relative motion model (16) under Assumptions 1 and 2 for autonomous landing missions. The adaptive sliding mode controller (30) and corresponding adaptive laws in (34) can ensure that tracking errors of closed-loop control system converge to zero and estimation errors of unknown parameters are uniformly bounded.

*Proof:* Since $V(t)\geq 0$ and $\dot{V}(t)\leq 0$, then $\dot{V}(t)$ is monotonically decreasing along the closed-loop control system trajectory and is bounded by zero. Hence, $V(t)$ have a finite limit $V(\infty)$ as $t\to\infty$, and satisfies $0\leq V(\infty)\leq V(t)\leq V(0)<\infty, \forall t\geq 0$. Meanwhile, by integrating both sides of Eq. (35), we have

$$
\int_0^{\infty}\|\boldsymbol{s}\|^2dt\leq-\frac{1}{\mu}\int_0^{\infty}\dot{V}(t)\mathrm{d}t\leq\frac{V(0)}{\mu}<\infty \tag{36}
$$

This means that $\boldsymbol{s}(t)$ is square integrable. From the definition of $V(t)$ in (26), we know

$$
0\leq\frac{1}{2}\mu\|\boldsymbol{s}\|^{\mathbf{2}}+\frac{1}{2}\gamma\|\boldsymbol{\chi}\|^2\leq V(t)<\infty \tag{37}
$$

where $\boldsymbol{\chi}\triangleq[\tilde{\boldsymbol{\vartheta}}_{\Delta}^{T},\tilde{\boldsymbol{\varphi}}_{\Delta}^{T},\tilde{d}_m]^T$, $\gamma\triangleq\max\{\gamma_1,\gamma_2,\gamma_2\}$. Thus, $\|\boldsymbol{s}\|<\infty$, and $\|\boldsymbol{\chi}\|<\infty$. From $\|\boldsymbol{s}\|<\infty$, and (20), we have $\|\tilde{\boldsymbol{x}}_1\|<\infty$; from (16) and $\|\boldsymbol{R}_{b}^{e}\|=1$, we know $\|\boldsymbol{x}_2\|<\infty$; from $\|\boldsymbol{\chi}\|<\infty$, we can obtain $\|\tilde{\boldsymbol{\vartheta}}_{\Delta}\|<\infty$, $\|\tilde{\boldsymbol{\varphi}}_{\Delta}\|<\infty$, $|\tilde{d}_m|<\infty$. Then, from (30), we have $\|\boldsymbol{u}\|<\infty$. Moreover, from (25), we know $\|\dot{\boldsymbol{s}}\|<\infty$. This imply that $\boldsymbol{s}(t)$ is uniformly continuous. Based on the Barbalat Lemma, we prove $\lim_{t\to\infty}\boldsymbol{s}(t)=0$. Furthermore, using the fact that the transfer function between $\boldsymbol{s}(t)$ and $\tilde{\boldsymbol{x}}_1(t)$ is strictly proper and exponentially stable, from (20) and $\lim_{t\to\infty}\boldsymbol{s}(t)=0$, we have $\lim_{t\to\infty}\tilde{\boldsymbol{x}}_1(t)=\lim_{t\to\infty}\dot{\tilde{\boldsymbol{x}}}_1(t)=0$.

*Remark 4:* Basing on adaptive sliding mode technique, the relative motion controller is presented in this work. Based on the estimations $\hat{\vartheta}_{\Delta},\hat{\varphi}_{\Delta},\hat{d}_m$, the adaptive sliding mode controller can be derived. There are four control inputs in this system model. The thrust $\delta_T$ and the elevator $\delta_e$ are coupled to control the longitudinal direction. The aileron $\delta_a$ and the rudder $\delta_r$ are coupled to control the lateral direction. The relative motion model (16) and the adaptive sliding mode control law (30) can be used to calculate the variations of system states and online estimations in the current sampling time. Then by using the Euler integral method, all system states and estimations in the next sampling time can be derived. Thus, the iteration of closed-loop control systems can be realized step by step.

**TABLE 1. Initial values in simulation.**

| variable | Value | Unit |
|---|---|---|
| $\boldsymbol{p}_a^E$ | $[-200,\ 10,\ 108]^{\mathrm{T}}$ | m |
| $\boldsymbol{\Theta}_a^E$ | $[1,\ 8,\ 0]^{\mathrm{T}}$ | deg |
| $\boldsymbol{\upsilon}_a$ | $[90,\ 0,\ 0]^{\mathrm{T}}$ | m/s |
| $\boldsymbol{\Omega}_a$ | $[0,\ 0,\ 0]^{\mathrm{T}}$ | rad/s |
| $\boldsymbol{p}_s^E$ | $[0,\ 0,\ 0]^{\mathrm{T}}$ | m |
| $\boldsymbol{\Theta}_s^E$ | $[0,\ 0,\ 0]^{\mathrm{T}}$ | deg |
| $\boldsymbol{\upsilon}_s$ | $[10,\ 0,\ 0]^{\mathrm{T}}$ | m/s |
| $\boldsymbol{\Omega}_s$ | $[0,\ 0,\ 0]^{\mathrm{T}}$ | rad/s |

## IV. SIMULATION EXAMPLE

In this section, simulation describe an example of the autonomous UAV carrier landing missions, in which the carrier has a lower dynamic operation condition so that the landing can be carried out safely [28]. After the relative position and relative attitude have been precisely controlled, the UAV and carrier will be well aligned without relative motions. Simulation results are demonstrated the performance of the developed controller. The initial simulation values are shown in Table 1. The desired relative position for autonomous UAV carrier landing in frame $\mathbb{F}_g$ is $\boldsymbol{x}_1^c=[0, 108-u_a\times\tan(\gamma_0)t, 0°, 4°]$, where is glide angle $\gamma_0=3°$. The Initial values of the adaptive parameters are set as $\hat{\boldsymbol{\vartheta}}(0)=[-183, 47, 288, 118, 295, -4390, -143, -1095, 938, 642.1, -619.58, -2345, 27.81, -247.1, 9390]$, $\hat{\boldsymbol{\varphi}}(0)=[10, 4, -3, 100, 81.8, -104, -98.7, -83.3, 0, -121.5]$. The controller parameters are selected as $\boldsymbol{k}_1=\mathrm{diag}\{10, 15, 4, 5\}$. The external disturbances on UAV are

$$
\boldsymbol{d}_{\tau s}=\begin{bmatrix}1+\sin(0.02t)+\sin(0.13t)\\1+\cos(0.1t)+\cos(0.11t)\end{bmatrix}\times 10^2(\mathrm{Nm}) \tag{38}
$$

$$
\boldsymbol{d}_{fs}=\begin{bmatrix}1+\sin(0.1t)+\sin(0.12t)\\1+\cos(0.09t)+\cos(0.14t)\end{bmatrix}\times 10^2(\mathrm{N}) \tag{39}
$$

Considering the medium sea condition in carrier dynamics, the carrier vertical motion coefficients are set as $\zeta_1=3.22$, $\zeta_2=1.305$, $\omega_1=0.6$, $\omega_2=0.2$; pitching motion coefficients are set as $\zeta_3=2.5$, $\zeta_4=3.0$, $\omega_3=0.5$, $\omega_4=0.52$, $b_1=0.5$; rolling motion coefficients are set as $\zeta_5=0.5$, $\zeta_6=0.30$, $\omega_5=0.6$, $\omega_6=0.63$, $b_2=0.25$.

To test the performance of control strategy designed in the last section, simulations for carrier following are implemented by Matlab. All values of parameters [29]–[32] used in simulations are demonstrated in Table 2.

The lateral channel is mainly responsible for maintaining the stability of the positions and attitudes in lateral directions. The lateral relative position $y_e$, velocity $v_e$ are depicted

**TABLE 2.** Parameters for the UAV and controller.

| Parameter | Value | Parameter | Value |
|---|---|---|---|
| $\rho$ | $0.088kg/m^3$ | $X_{\delta_T}$ | 24287 |
| $m_a$ | $11347kg$ | $X_{\delta_e}$ | 358.25 |
| $g$ | $9.8kg/m^3$ | $Y_{\delta_a}$ | 266.3 |
| $I_x$ | 12875 | $Y_{\delta_r}$ | 727.05 |
| $I_y$ | 75674 | $Z_{\delta_T}$ | 0 |
| $I_z$ | 85552 | $Z_{\delta_e}$ | $-1927.5$ |
| $I_{zx}$ | 1331 | $L_{\delta_a}$ | $-6004.1$ |
| $X_u$ | $-52.33$ | $L_{\delta_r}$ | 1081.8 |
| $X_w$ | 498.76 | $M_{\delta_e}$ | 0 |
| $X_q$ | 2868.1 | $M_{\delta_T}$ | $-8721.5$ |
| $Y_v$ | $-1383.9$ | $N_{\delta_a}$ | $-1083.3$ |
| $Y_p$ | 647.65 | $N_{\delta_r}$ | $-3598.7$ |
| $L_v$ | $-1543$ | $L_p$ | $-21095$ |
| $L_r$ | 5938.2 | $N_v$ | 2642.1 |
| $N_p$ | $-719.58$ | $N_r$ | $-20345$ |

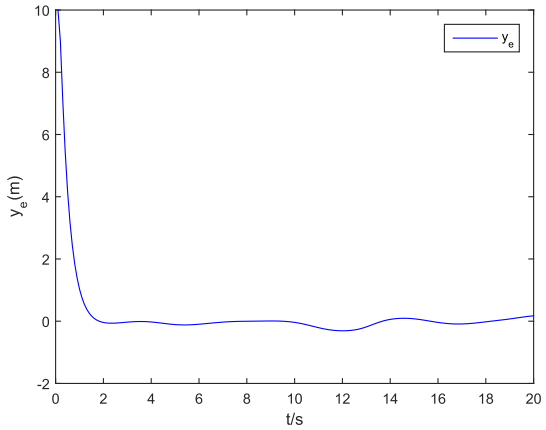


**FIGURE 2.** The relative lateral position ($y_e$) error.

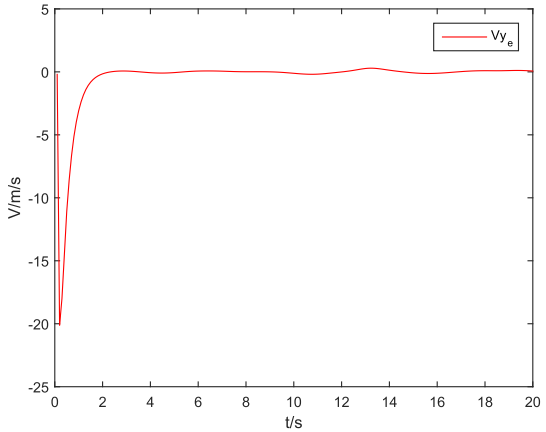


**FIGURE 3.** The relative lateral velocity ($v_e$) error.

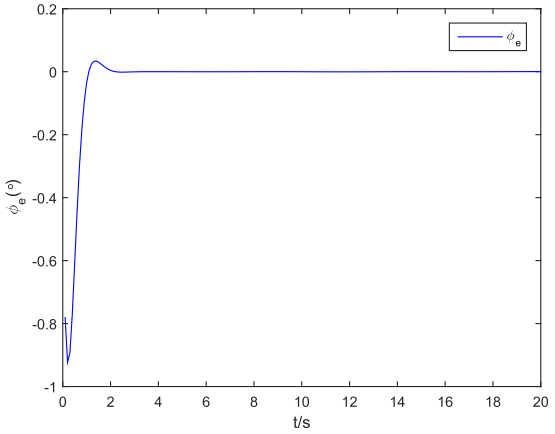


**FIGURE 4.** The relative rolling ($\phi_e$) motion error.

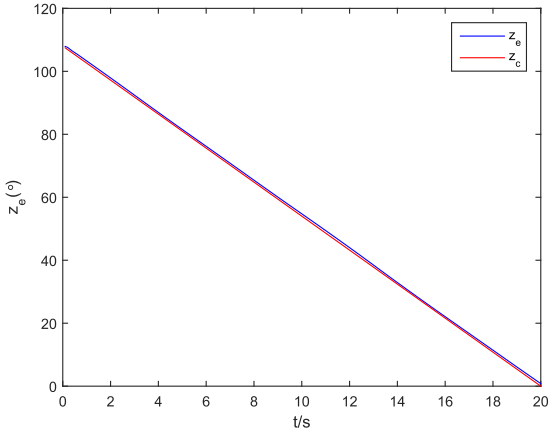


**FIGURE 5.** The relative vertical position ($z_e$) and desired vertical position($z_e^c$).

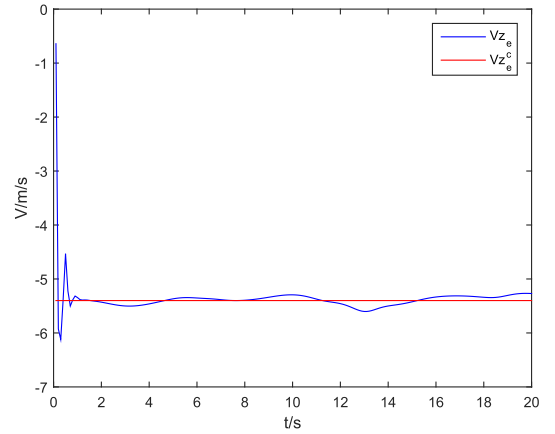


**FIGURE 6.** The relative vertical velocity ($w_e$) and desired vertical velocity ($w_c$).

in Fig. 2 and Fig. 3, which ensure that the UAV does not deviate from the carrier's runway. the relative attitude $\phi_e$ and angular velocity $p_e$ shown in Fig. 4 are converged to zero, which avoid from rolling, because the unstable roll angle can cause the UAV to deviate from the setting course. According to Fig. 5, it is shown that the desired landing objective is reached in about 20(s) and the relative vertical velocity goes to $-5.49$(m/s) depicted in Fig. 6, which ensure the stability of decline rate. According to Fig. 7, it is shown that the

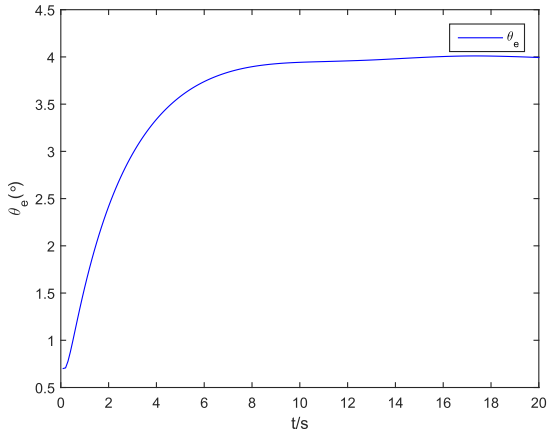


**FIGURE 7.** The relative pitching ($\theta_e$) motion error.

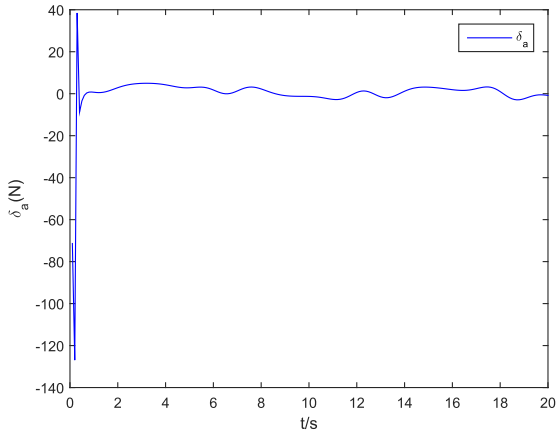


**FIGURE 10.** The system aileron control inputs ($\delta_a$).

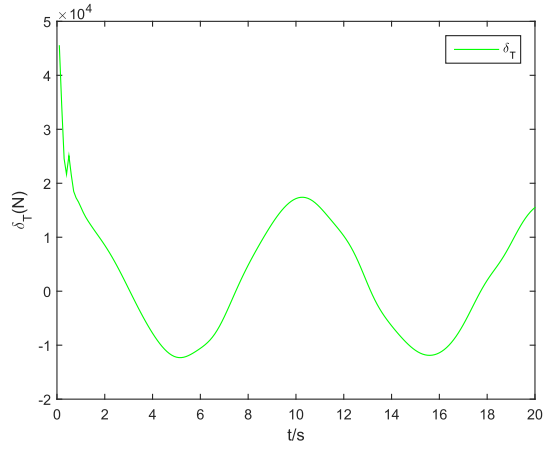


**FIGURE 8.** The system trust control input ($\delta_T$).

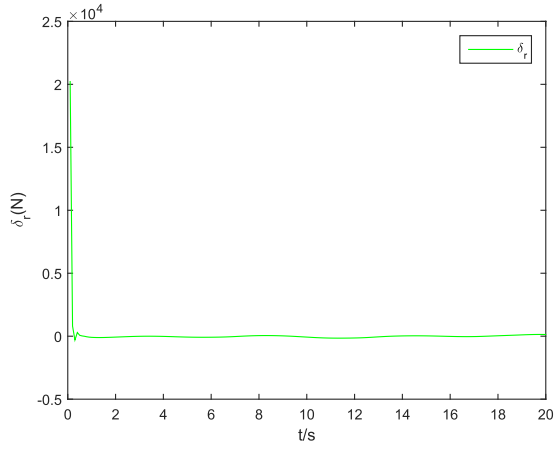


**FIGURE 11.** The system rudder control inputs ($\delta_r$).

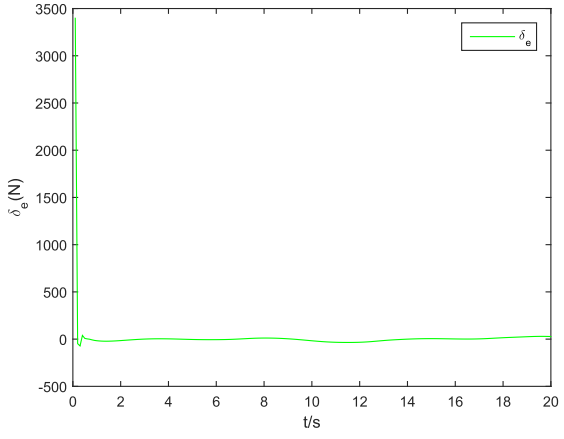


**FIGURE 9.** The system elevator control input ($\delta_e$).

desired relative pitch angle goes to 4°. This shows that the pitch angle, between UAV and carrier, maintain the 4° angle. It's mean that the UAV, during the process of landing carrier, can make sure to go around which forbid anything that might happen [33], [34].

Meanwhile, the control thrust $\delta_T$ presented in Fig. 8 shows that the initial control input are large and appears a fluctuation during the process of carrier landing. In order to keep up with the movement of the aircraft carrier for desired position and attitude, UAV's thrust needs adjust constantly.

In order to drive the UAV to the desired position and attitude quickly, the control forces and torques presented in Fig. 9, Fig. 10 and Fig. 11 show that the initial control inputs are large. It decreases rapidly after the desired position and attitude is achieved.

## V. CONCLUSION

A adaptive sliding mode control method was proposed for autonomous UAV carrier landing in this work. The external disturbances, dynamic coupling effect and uncertain aerodynamic parameters are considered simultaneously in 4-DOF integrated controller design. The adaptive sliding mode control scheme can deal with a large amount of unknown parameters in the coupled dynamics and achieve linear parameters estimation. Two degrees of freedom in forward and yaw directions are ignored, because the UAV is the fixed wing aircraft which is an under actuated system. In addition, due to the flight characteristics of fixed wing, maintaining a constant vertical velocity, the UAV can also meet the corresponding

constant forward velocity. Thus, the forward position can be obtained indirectly in the given time. Similarly, while UAV maintain a constant lateral displacement, the control of the yaw angle is also satisfied to the desired target. Therefore, the demands of control law can be satisfied. The presented controller is able to drive UAV to the desired trajectory and attitude accurately in approach of carrier landing.Simulation example is shown to demonstrate excellent performance. Future works will focus on the more practical problem by extending the experimental method in this work.

## REFERENCES

[1] H. B. Duan, Y. X. Yu, and Z. Y. Zhao, "Parameters identification of UCAV flight control system based on predator-prey particle swarm optimization," *Sci. China Inf. Sci.*, vol. 56, no. 1, pp. 1–12, Jan. 2013.
[2] Y. Deng and H. Duan, "Control parameter design for automatic carrier landing system via pigeon-inspired optimization," *Nonlinear Dyn.*, vol. 85, no. 1, pp. 1–10, 2016.
[3] J. Li and H. Duan, "Simplified brain storm optimization approach to control parameter optimization in F/A-18 automatic carrier landing system," *Aerosp. Sci. Technol.*, vol. 42, pp. 187–195, Apr./Mar. 2015.
[4] D. Ito and J. Valasek, "Robust dynamic inversion controller design and analysis for the X-38," in *Proc. AIAA Guid., Navigat. Control Conf. Exhibit*, Montreal, QC, Canada, 2001, p. 4380.
[5] A. Tsourdos, D. J. Leith, W. E. Leithead, and B. A. White, "A velocity-based framework for the robust stability analysis of dynamic inversion flight controllers," in *Proc. Amer. Control Conf.*, Jun. 2001, vol. 5. no. 5, pp. 3341–3345.
[6] U. Ali, "Robust level flight control design for scaled Yak-54 unmanned aerial vehicle using single sliding surface," in *Proc. Control Decision Conf. (CCDC)*, May 2012. vol. 229, no. 5, pp. 1209–1214.
[7] X. Gao, Y. Fang, and Y. Wu, "Fuzzy Q learning algorithm for dual-aircraft path planning to cooperatively detect targets by passive radars," *J. Syst. Eng. Electron.*, vol. 24, no. 5, pp. 800–810, Oct. 2013.
[8] Y. Fan and X. Y. Meng, "Control allocation for a V/STOL aircraft based on robust fuzzy control," *Sci. China Inf. Sci.*, vol. 54, no. 6, pp. 1321–1326, 2011.
[9] M. B. Subrahmanyam, "H-infinity design of F/A-18A automatic carrier landing system," *J. Guid. Control Dyn.*, vol. 17, no. 1, pp. 187–191, 1994.
[10] B. Morton, D. Enns, and B. Y. Zhang, "Stability of dynamic inversion control laws applied to nonlinear aircraft pitch-axis models," *Int. J. Control*, vol. 63, no. 1, pp. 1–25, 2007.
[11] J. Yothi, G. R. Bindu, and M. Jayakumar, "Robust longitudinal controller design for an unmanned tailless aircraft," in *Proc. AiAA Aviation Technol., Integr. Oper. Conf.*, 2006, p. 7792.
[12] A. Hashem, "Review of nonlinear tracking and setpoint control approaches for autonomous underactuated marine vehicles," in *Proc. Amer. Control Conf. (ACC)*, Jul. 2010. vol. 58, no. 8, pp. 5203–5211.
[13] L. Sun and W. Huo, "Robust adaptive relative position tracking and attitude synchronization for spacecraft rendezvous," *Aerosp. Sci. Technol.*, vol. 41, pp. 28–35, Feb. 2015.
[14] T. Cimen and S. P. Banks, "Nonlinear optimal tracking control with application to super-tankers for autopilot design," *Automatica*, vol. 40, no. 11, pp. 1845–1863, 2004.
[15] K. Y. Pettersen and H. Nijmeijer, "Tracking control of an underactuated surface vessel," *Decision Control*, vol. 4, no. 4, pp. 4561–4566, 1998.
[16] L. Sun and W. Huo, "Robust adaptive control of spacecraft proximity maneuvers under dynamic coupling and uncertainty," *Adv. Space Res.*, vol. 56, no. 10, pp. 2206–2217, 2015.
[17] B. L. Cong and X. D. Liu, "Backstepping based adaptive sliding mode control for spacecraft attitude maneuvers," *Aerosp. Sci. Technol.*, vol. 30, no. 1, pp. 1046–1051, 2012.
[18] Z. Zheng and Y. Zou, "Adaptive integral LOS path following for an unmanned airship with uncertainties based on robust RBFNN backstepping," *ISA Trans.*, vol. 65, pp. 210–219, Nov. 2016.
[19] W. Meng, Q. Yang, S. Jagannathan, and Y. Sun, "Adaptive neural control of high-order uncertain nonaffine systems: A transformation to affine systems approach," *Automatica*, vol. 50, no. 5, pp. 1473–1480, 2014.
[20] Y. L. Xiao, *Aircraft Motion Equation*. BeiJing, China: Aviation Industry Press, 1987, pp. 13–20.
[21] W. Dong and Y. Guo, "Nonlinear tracking control of underactuated surface vessel," in *Proc. Amer. Control Conf.*, vol. 6. 2005, pp. 4351–4356.
[22] A. Khan, C. Bil, and K. E. Marion, "Ship motion prediction for launch and recovery of air vehicles," in *Proc. MTS/IEEE OCEANS*, vol. 3. Sep. 2005, pp. 2795–2801.
[23] Z. Zheng and L. Sun, "Path following control for marine surface vessel with uncertainties and input saturation," *Neurocomputing*, vol. 177, pp. 158–167, Feb.2016.
[24] M. Zhu and Z. H. Jin, "Relative motion modeling and control for Autonomus UAV carrier landing," in *Proc. Chin. Control Decision Conf. (CCDC)*, May 2016, pp. 6415–6421.
[25] K. Lu and Q. Li, "An autonomous carrier landing system design and simulation for unmanned aerial vehicle," in *Proc. Guid. Navigat. Control Conf. (CGNCC)*, May 2014, pp. 1352–1356.
[26] W. Meng, Q. Yang, and Y. Sun, "Guaranteed performance control of DFIG variable-speed wind turbines," *IEEE Trans. Control Syst. Technol.*, vol. 24, no. 6, pp. 2215–2223, Nov. 2016.
[27] Y. Shtessel, C. Edwards, and L. Fridman, "Sliding mode control and observation," *Int. J. Control*, vol. 9, pp. 213–249, 2016.
[28] J. Bošković and J. Redding, "An autonomous carrier landing system for unmannned aerial vehicles," in *Proc. AIAA Guid. Navigat. Control Conf.*, 2009, p. 6264.
[29] P. Sousa, L. Wellons, J. Waters, and J. Weir, "Test results of an F/A-18 automatic carrier landing using shipboard relative global positioning system," *Int. J. Mech. Mater. Design*, vol. 7, no. 1, pp. 29–44, 2003.
[30] A. L. Prickett and C. J. Parkes, "Flight testing of the F/A-18E/F automatic carrier landing system," in *Proc. IEEE Aerosp. Conf.*, vol. 5. Mar. 2001, pp. 2593–2612.
[31] K. E. Awenzel, A. Masselli, and A. Zell, "Automatic take off, tracking and landing of a miniature UAV on a moving carrier vehicle," *J. Intell. Robot. Syst.*, vol. 61, no. 1, pp. 221–238, 2011.
[32] S. Saripalli, J. F. Montgomery, and G. S. Sukhatme, "Vision-based autonomous landing of an unmanned aerial vehicle," in *Proc. IEEE Int. Conf. Robot. Autom. (ICRA)*, vol. 3. May 2002, pp. 2799–2804.
[33] B. L. Stevens and L. Frank, "Aircraft control and simulation," in *Aircraft Engineering Aerospace Technology An International Journal*, 2nd ed. 2003.
[34] J. F. Sweger, "Design specifications development for unmanned aircraft carrier landings: A simulation approach," USNA, Annapolis, MD, USA, Tech. Rep. 2003.

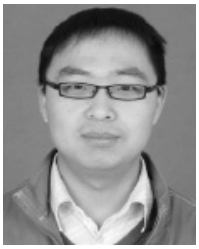

**ZEWEI ZHENG** received the B.S. degree in automatic control from the Beijing Institute of Technology, Beijing, China, in 2006, and the Ph.D. degree in control theory and control engineering from Beihang University, Beijing, China, in 2012. He was a Post-Doctoral Fellow with Beihang University from 2012 to 2014, where he is currently an Assistant Professor with the School of Automation Science and Electrical Engineering. His research interests include nonlinear control system, flight control, and motion control.

**ZHENGHAO JIN** received the bachelor's degree in engineering mechanics in 2013. He is currently pursuing the master's degree with the School of Aeronautic Science and Engineering, Beihang University. His research interests include nonlinear mechanical system control, carrier landing control, and unmanned aerial vehicle control.

**LIANG SUN** (M'16) received the M.Sc. and Ph.D. degrees in control theory and control engineering from Beihang University, China, in 2011 and 2015, respectively. He is currently a Post-Doctoral Fellow with the School of Automation Science and Electrical Engineering, Beihang University. His research interests include nonlinear mechanical system control, spacecraft control, and unmanned aerial vehicle control.

**MING ZHU** received the M.Sc. and Ph.D. degrees in aircraft design from Beihang University, Beijing, China, in 1998 and 2006, respectively. He was a Post-Doctoral Fellow with Beihang University from 2006 to 2007, where he is currently a Professor with the School of Aeronautic Science and Engineering. His research interests include solar unmanned aerial vehicles and unmanned aerial vehicle structure optimization.